Research Article

Thomas Scholz*, Martin Laurenzis and Frank Christnacher

Laser-based imaging applications in turbid waters

https://doi.org/10.1515/aot-2019-0033
Received May 23, 2019; accepted September 9, 2019; previously published online September 28, 2019

Abstract: Underwater laser-based imaging systems and data-processing techniques matured during the past decade. Active imaging systems can, nowadays, be integrated into platforms like remote-operated vehicles (ROV) or autonomous underwater vehicles (AUV). This article gives an overview of different civil and naval applications in underwater imaging with respect to underwater laser scanning (ULS) and laser gated viewing (LGV). Special emphasis has to be given to the environmental conditions, for example, the influence of the local and seasonal dependence of the turbidity with regard to the optical underwater channel. On the basis of tank and sea experiments, advanced techniques for 3D laser oblique scanning (LOS) and possibilities of contrast enhancements for gated viewing are presented.

Keywords: laser gated viewing; laser scanner; post-processing; underwater laser imaging.

1 Introduction

Many advanced underwater laser scanning (ULS) and laser gated viewing (LGV) applications based on military demonstrators emerged in the 1990s (cf., e.g. Ref. [1]). Underwater 3D active imaging is recognized as a beneficial technology to identify objects like mines or dumped ammunition lying on the seafloor in comparison to sonar systems with their limited spatial resolution. Additionally, for mine hunting in some countries, an optical identification of sea mines is mandatory. Among other civil applications, some address, e.g. pipeline or sea cable inspection. In the same time period of the 1990s, electronic devices like fast shutters and cameras on the basis of charged coupled devices or streak tubes matured. Since about 2010, ULS systems are more widely spread on the free market, and a new class of scanners with red, green, and blue laser sources (RGB-ULS) for true color applications emerged [2].

Typically, modern synthetic aperture sonars (SASs) are integrated into autonomous underwater vehicles (AUV) together with high-quality micronavigation systems for underwater imaging applications. Linear SAS systems reach spatial resolutions of some centimeters to detect and classify objects or to produce digital charts of the seafloor. On the other hand, especially continuous wave (cw) laser scanners realize higher spatial resolutions of some millimeters and are more sensitive to color contrasts, compared to sonars. Active gated cameras are beneficial in environments with changing illumination due to the use of intensive and short to ultra-short laser pulses [3]. Today, the first combinations of SAS and ULS systems are integrated into AUVs for naval and civil applications.

In this paper, we compare ULS and LGV and give a brief overview of the different applications of these active underwater imaging technologies. Finally, we summarize the outcome of both approaches and discuss the advantages and drawbacks of these methods.

2 Optical properties of the submarine environment

Both mine hunting applications and the identification of dumped ammunition takes place close to the shore at moderate water depths. In shallow waters, tidal currents or the wind-driven sea lead to a transport of sediment in the water column increasing the number of light scattering particles per volume element. Organic matter, like algae, populates the water column up to the daylight limit. The dyes included in this organic matter absorb light, preferably in the red and blue spectral range. For this reason, a lot of laser-based underwater sensors use green light for

***Corresponding author: Thomas Scholz,** Technical Centre for Ships and Naval Weapons, Maritime Technology and Research (WTD 71), Berliner Str. 115, 24340 Eckernförde, Germany,
e-mail: ThomasScholz@bundeswehr.org
Martin Laurenzis and Frank Christnacher: French-German Research Institute of Saint-Louis (ISL), P.O. Box 70034, 68301 Saint-Louis Cedex, France

www.degruyter.com/aot

shallow water surveys. In the deep sea, the blue spectral range is often preferred.

The influence of scattering and absorption on underwater light propagation is described with the help of the radiative transfer equation (RTE) [4]. In the stationary case, one finds:

$$s \cdot \nabla L = -cL + RL + E \tag{1}$$

The term on the left-hand side represents the directional derivative of the radiance L with respect to the beam direction $\boldsymbol{s}$, $c = a + b$ is the attenuation, a is the absorption coefficient, and b is the scattering coefficient, which is the integral of the volume scattering function (VSF) over all angles [5]. R is an integral operator describing the backscattering of light from the surrounding water volume into the beam, and E is an external source like daylight. In the case of a homogeneous water volume and setting $R = E = 0$, one arrives at the Lambert-Beer's law of optical damping for a light beam traveling a straight distance r at wavelength λ:

$$I(r) = I(0)e^{-c(\lambda)r} \tag{2}$$

For a plane wave, radiance L corresponds to beam intensity I. The wavelength-dependent attenuation in different coastal regions at constant depth is depicted together with a scenario for a laser-based sensor integrated on an AUV in Figure 1. The attenuation coefficient was measured by WTD 71 with the help of a turbidity sensor at nine different wavelengths (Wet labs ac-9). For this reason, the system uses a rotating wheel with nine color filters and two different channels to measure attenuation and absorption in parallel. From the difference between attenuation and absorption, scattering can be calculated. The accuracy of the turbidity sensor amounts to ±0.01 m^{-1}. Attenuation varies from 0.09 m^{-1} at 450 nm in the Mediterranean Sea to 1.78 m^{-1} at 715 nm in Kiel Harbor.

Frequency doubled Nd:YAG-laser systems at 532 nm wavelength are often used in coastal underwater applications. From a lot of the corresponding underwater communications, LGV, and ULS experiments in the last years, we found a maximum visibility range, V, of about six attenuation lengths, $V = 6/c$. Attenuation was measured during different sea trials in the Baltic and Mediterranean Seas. For instance, $V = 3.4$ m at a wavelength of 715 nm at an attenuation of 1.78 m^{-1} in the Kiel Harbor or 67 m at a wavelength of 450 nm at an attenuation of 0.09 m^{-1} in the Mediterranean Sea. With respect to Figure 1, the visibility range in the green spectral range at 532-nm wavelength can be determined to 6.0 m for the Kiel Harbor, 12.8 m for the western Baltic Sea, and 43.1 m for the Mediterranean Sea. Further, the actual local weather can have tremendous impact on the attenuation coefficient in the water column. For instance, for the measurements in Kiel Harbor, we had had a sunny period on March 2011 for more than 2 weeks before the attenuation measurement took place ($c = 1.0$ m^{-1}), so that cold-water algae populated the water column. Later, there were other measurements in July, where we measured $c = 0.8$ m^{-1} at the same place. For the characterization of the mine model in Ref. [3], attenuation in the open Baltic Sea was found to be 0.47 m^{-1}, due to the fact that due to cloudy and rainy weather conditions

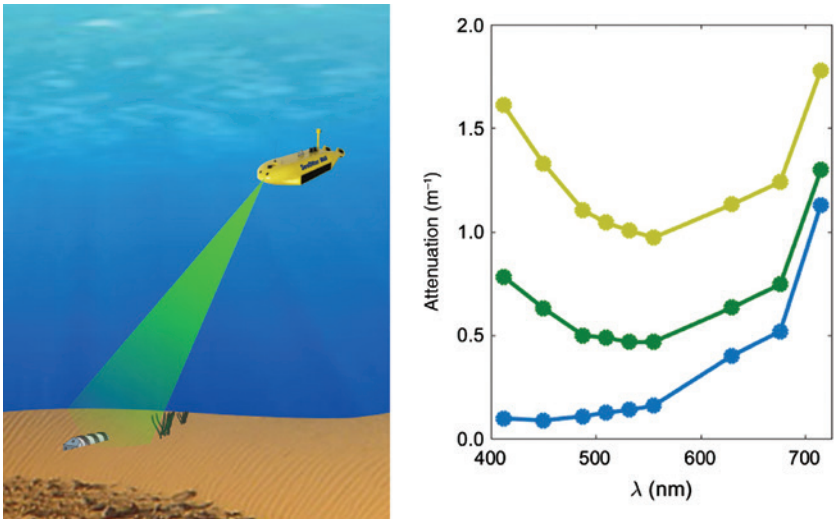

Figure 1: Left: An optical sensor integrated on an AUV scans the seafloor for a ground mine, which is partially sunk or can be hidden by sea grass. Right: Attenuation coefficient c(λ) at 5-m water depth. Blue: Mediterranean Sea near Sardinia (June). Dark Green: Western Baltic Sea near Damp (March). Light Green: Kiel Harbor (March).

throughout the first quarter of 2014, algae concentration was moderate.

Multiple scattering of light acts more destructive than absorption, a fact that can be taken into account by the optical albedo $\omega_0 = b/c$ [6] as the ratio of the scattering coefficient to the attenuation coefficient. In the first three cases, we found, for the albedo, 0.55 (Kiel Harbor), 0.66 (Baltic Sea), and 0.40 (Mediterranean Sea) at 532 nm. Although scattering and absorption play the most important role in turbid coastal waters, also turbulence can degrade the imaging process [7] due to currents involved or in certain layers, where strong variations in the depth dependence of temperature and salinity occur. An increase in the attenuation can also be found near the seafloor when the wind-driven sea is able to stir up particles forming ripple structures at water depths up to 10 m.

3 Underwater laser oblique scanning

Laser oblique scanning (LOS) is a 3D imaging method that uses an array detector to image and to analyze the deformation of the laser line illumination by the observed target. The spatial resolution increases by scanning and observation of only small solid angles by thin laser beams. From terrestrial applications, the benefit of oblique scanning is well known, relying on one imaging sensor scanning a scene from two or more directions or multiple sensors with different angles of incidence. LOS helps to avoid shadow regions or allows to remove the influence partial occlusion, e.g. if a floor structure is hidden by a forest [8].

Underwater, this can be achieved with laser scanners generating dense 3D point clouds. The ULS shown in Figure 2 is a cw system from 2G Robotics based on the principle of triangulation. It measures the angle of backscattered light and consists of a line scanner with a laser source at 532 nm wavelength, 5-mW laser beam power, and a spatially separated sensor. The head of the scanner can be rotated with a minimum step size of 0.018° at $n \cdot 360°$. The resolution of the detector array is 480 pixels or 0.104° at an aperture of 50°. For an object at a distance of 0.5 m, the theoretical spatial resolution equals 0.16 mm horizontally and 0.97 mm vertically. The scanner was integrated into a cubic frame with a length of 1 m. The frame can be lowered into the water column with the help of a crane. It also consists of a sand-colored ground plate with three objects to simulate the environment of the seafloor. The plate can be positioned in different heights with respect to the scanner head. The maximum height of the artificial plants is 23 cm. The scan angle of incidents amounts to ±11.3° and results from a scan height above the plate of 50 cm and a lateral offset of ±10 cm. The measurements were performed in a water tank at a high attenuation of 1.0 m^{-1}. The water tank was located in a hall with daylight coming in through small windows. So external light intensity was moderate.

The scattering positions (x, y, z) are stored in two files for the two separate positions of the scanner and are plotted for a selected volume of $35 \times 12 \times 25$ cm^3 in Figure 3A and B. Both point clouds were added (Figure 3C) and consist in total of about 88 000 scattering coordinates. In a final step, a volume scattering filter was applied (Figure 3D). The filter is based on the assumption that the scatterings from the surfaces involved are dense compared to the occurring volume scattering. If inside a sphere of

Figure 2: From left to right: ULS-100 system owned by WTD 71, frame with an edge length of 1 m, artificial plants enclosing a shell on the sand-colored bottom plate of the frame, and principle of LOS. The ULS on the left consists of the lower part of the sensor head and of the upper part of a cylinder containing a stepping motor for rotating the sensor head. The sensor head is equipped with the laser line scanner on the left and the camera optics on the right-hand side.

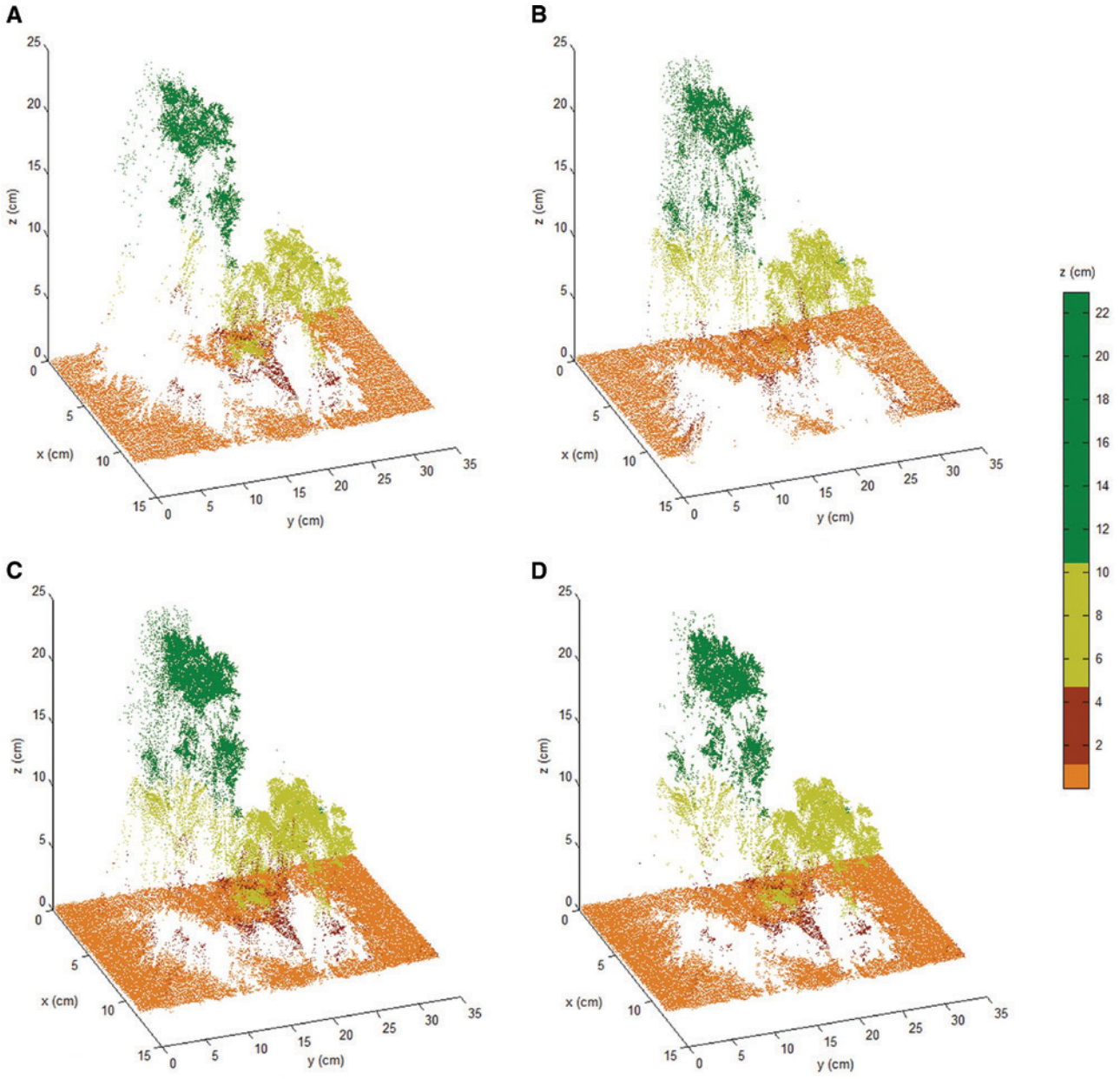

Figure 3: Scan from the front (A), scan from behind (B), added point clouds (C) with reduced shadow regions of the scene, and volume scattering filter applied (D).

a characteristic radius from the scattering position under consideration no other scatterings occur, this element is excluded as a surface scattering. The radius of the sphere was set to 1.5 mm, 50% above the theoretical spatial resolution of the ULS. Runtime on a conventional notebook for the filter is about 3 min without optimizations, and here, 8.1% of the volume scatterings were removed.

The coloring is done with respect to different classes for the height structure found. The class for the lowest structure refers to the flat seafloor simulated by the plate, the second to structures like the shell directly placed on the floor, the third to the lower, and the fourth to the higher vegetation structure.

4 Underwater laser-gated viewing

LGV systems are based on short to ultra-short laser pulses and have the advantages to deliver a live video stream and to collect only the reflected light from a predefined range gate [9]. Gated viewing filters the returning signal

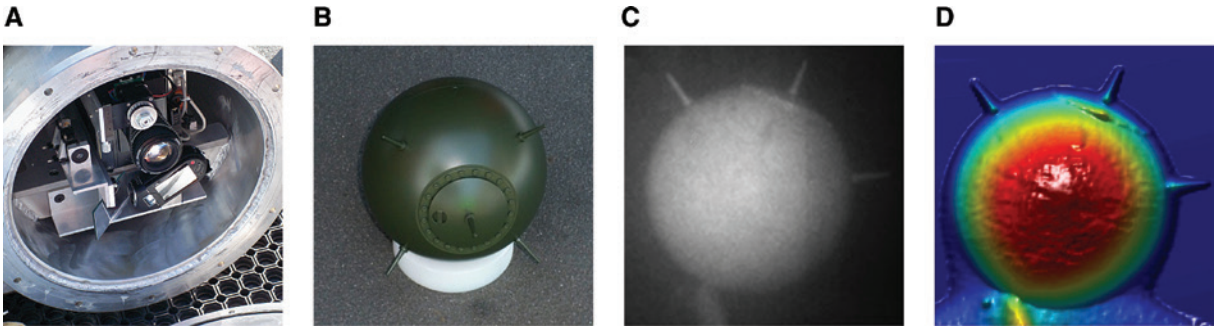

Figure 4: LGV system of ISL (A) integrated into a water-resistant housing, (B) mine model of WTD 71, (C) 2D intensity image of the reflected light underwater, and (D) post-processed 3D reconstruction of the mine model.

temporally and suppresses the contribution of scattered light to the imaging process. The minimal gate interval of the system from the French-German Research Institute of Saint-Louis (ISL) shown in Figure 4A amounts to 2 ns. The system relies on a Nd:YAG micro-chip laser at 532-nm wavelength with a pulse duration of 0.5 ns and a pulse repetition frequency of 1 kHz. Pulse energy equals 10 µJ or a mean optical power of 10 mW. The camera consists of a digital intensified charged coupled device (ICCD) with an exposure time of 0.5 ns.

During an experiment of WTD 71 and ISL in the Baltic Sea, the LGV system was used together with the model of a spherical sea mine with a diameter of 20 cm (cf. Figure 4B). The original dark green painting is characterized by a reflectance of 9% at 532 nm. Because of the presence of cold-water algae the attenuation coefficient at the laser wavelength was high and determined as 1.0 m^{-1}. The picture in Figure 4C shows the image of the mine taken underwater with the ICCD camera at a range of 3 m to the mine model. Further, 3D data were recorded by tomography with a sliding range gate and 31 delays at a step size of 0.1 ns.

By varying the reference time, before the shutter of the camera is opened, a 3D picture of the scene can be calculated (Figure 4D). In this case, we applied a global contrast enhancement (GCE) algorithm [10] for improvement avoiding visual artifacts. By correlation of the LGV image with a 3D computer model of the object, an effective spatial resolution of 9 mm was calculated for the system. The maximum visibility range of the LGV system was estimated to be about five attenuation lengths or $5.2/c$ (compare performance in fog tunnel [11]).

For comparison, in Figure 5, the 3D mapping results measured with the ULS are depicted. This figure illustrates the recorded point cloud and a reconstructed surface model. The UlS obtained a resolution of about 1 mm. It is obvious that the ULS was operated with very high sampling resolution to obtain a maximum point cloud density. In this operation mode, the ULS system obtains a much higher spatial resolution, but needed several minutes to sample the volume. On the other hand, the LGV system operated with a single fixed spatial resolution, which is mainly defined by the array size. At these conditions, LGV obtained a resolution on the cm scale, but at video frame rate.

In another experiment, we integrated the LGV system on a slowly moving underwater vehicle (UV) to monitor the seafloor. We recorded a series of 15–20 images with a sensor gate delay step size of 0.2 m. Because of the nonstationary position of the UV, we had to compensate image motion using a feature detection and image registration algorithm [9].

Figure 6 depicts an example for a seafloor observation. In Figure 6A, the image data and the registration and stitching process are represented for two images of an LGV tomography sequence. In Figure 5B, transient data sequences (pixel intensities for different range gate positions) are shown for five different pixel positions (A, B, C, D, and E) of the registered images. The range and

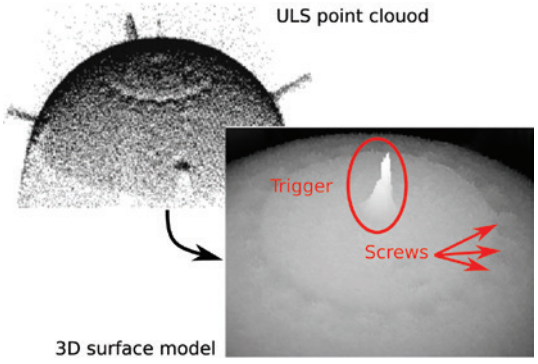

Figure 5: The 3D point cloud and surface model of the mine model measured with the USL system.

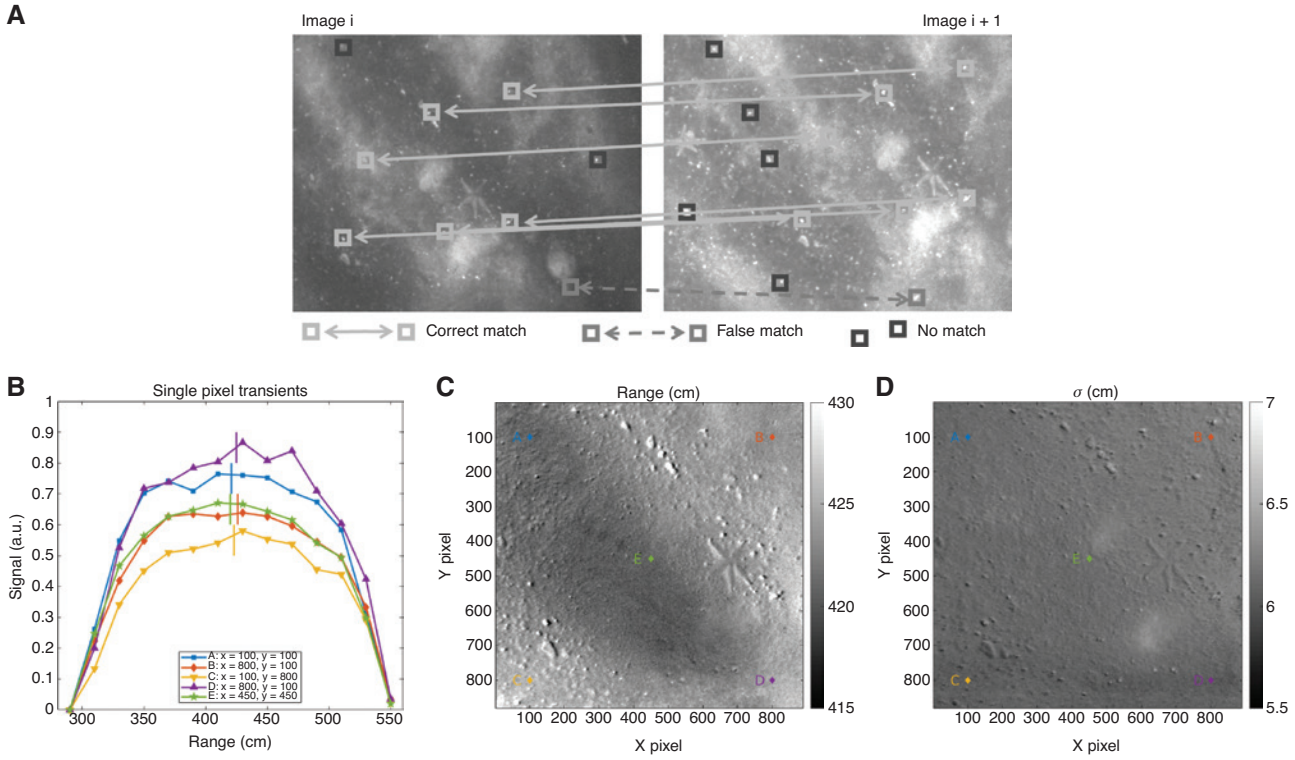

Figure 6: An example for 3D imaging from a moving platform using motion compensation. After registration (A) of the recorded intensity images, 3D range is reconstructed for each pixel from transient data (B) by calculating the weighted mean range (C) and standard deviation (D).

standard deviation are calculated from a weighted mean, as defined in Eq. (3) [12].

$$\hat{z} = \frac{\sum_{i=1}^{n} z_i I_i}{\sum_{i=1}^{n} I_i} \quad \text{and} \quad \sigma = \sqrt{\hat{z}^2 - \hat{z}^2} \quad \text{with} \quad \hat{z}^2 = \frac{\sum_{i=1}^{n} z_i^2 I_i}{\sum_{i=1}^{n} I_i}. \tag{3}$$

In this experiment, we observe the seafloor at a range of 415–430 cm with a standard deviation of about $\sigma = 6$ cm. The range image (Figure 5C) shows the surface topography (long scale: ripples, short range: stones) and further details (e.g. a sea star) can be figured out. Although, the standard deviation does not directly depend on the measured intensity values, we observe a variation of this values at the edge of objects (e.g. stones), as illustrated in Figure 5D. This effect is linked to the image registration accuracy, which can be effected by the image quality (scattering blur) and pixel intensity variation within the range gate.

The obtained results demonstrate that we can obtain super-resolution depth profiling from a moving platform. Our underwater LGV system can be compared with state-of-the-art systems of other groups [13, 14]. For instance, these groups used a monochrome CMOS time-of-flight sensors and an illumination laser pulse power of 2 mJ (or 2 mW/image) at a frame rate of 400 Hz. As aforementioned, we used an ICCD sensor at a sensor frame rate of 20–25 Hz and a laser source of 10 µJ at 1 kHz. In each image, we accumulate the reflection of an optical illumination power of about 0.4 mW/image.

5 Discussion and conclusion

In our experiments, we compared the application of ULS and underwater LGV technologies. Both methods were proven to effectively deal with the challenges of the high scattering and attenuation in the underwater scenario. While ULS records data from a narrow laser beam in the whole imaging volume, the scattering signals are filtered out by analyzing the spatial distribution and density of the point cloud. On the other hand, LGV suppresses scattering signals by temporally filtering the reflected light during data recording.

In ULS, the application of laser oblique scanning from different angles can be used to reduce shadowing areas in the point cloud. Further, ULS proved the application of different point cloud densities and scanning areas (i.e. the field of regard). On the other hand, LGV has a fixed

field of view and illuminates the whole sensing area with a single highly divergent laser pulse. The 3D data can be obtained by analyzing an image sequence recorded with a varying or scanning range gate. To compensate motion in the images, an image registration, known from computer vision, has to be applied. Further, in principle, the LGV system can be used to reduce the shadow areas by adding point clouds from different viewpoints similar to the ULS system. Nevertheless, this was never demonstrated for underwater LGV and could be subject for research of future activities.

Further, depending on system parameters, LGV systems show a typical depth resolution of about 1 cm compared to 1 mm for ULS systems with appropriate basis length between scanner and camera at imaging ranges of a few meters underwater. Nevertheless, LGV systems deliver a live video stream that can be used for image-based navigation by an operator of remote-operated vehicles (ROV) or for automated navigation of an AUV.

The experiments also relied on the concept of the virtual ocean, which uses scaling factors for the experimental setup and the objects included. The scaling was typically set to a factor of 4 (e.g. size of a mine model) in our optical underwater studies compared to real world scenarios. This makes it possible to start in a test tank environment before going to the open sea and also helps to clarify the possibilities and restrictions of LOS and LGV sensor technology involved more easily.

Additionally, our scientific studies illuminate the influence of the environmental conditions in turbid waters, which are often more sophisticated than for atmospheric applications [9]. In a future international cooperation, there exist plans to use an airborne LIDAR system for object detection first and apply LOS and LGV from an ROV or an AUV for relocalization and identification purposes.

LOS has shown to reduce shadow regions and is able to generate a deeper look into partially hidden structures, while LGV realizes faster acquisition times and is beneficial in scenarios under the influence of varying daylight conditions. In extreme turbid water masses ($c > 2\ m^{-1}$ and $b > 1\ m^{-1}$), optical applications are limited to very short ranges of less than a few meters. Finally, for the future new technologies, LIDAR on a chip and VCSEL, compared, e.g. to circular SAS and acoustic camera applications, should also be taken under consideration.

References

[1] G. R. Fournier, D. Bonnier, J. L. Forand and P. W. Pace, Opt. Eng. 32, 2185–2190 (1993).
[2] Y. Yang, B. Zheng, L. Y. Kan, J. Yu, and J. C. Wang. Optik. 125, 6074–6077 (2014).
[3] M. Laurenzis, F. Christnacher, T. Scholz, N. Metzger, S. Schertzer, et al., Proc. SPIE 9250, 92500D-1 (2014).
[4] F. Hanson and S. Radic, Appl. Opt. 47, 277–283 (2007).
[5] N. G. Jerlov, Marine Optics, (Elsevier Oceanography Series 14, Amsterdam, The Nederlands, 1976).
[6] M. H. Niemz, Laser-Tissue interactions, (Springer, Berlin, Heidelberg, 1996).
[7] A. V. Kanaev, W. Hou, S. Woods and L. N. Smith, Opt. Eng. 51, 057007 (2012).
[8] M. A. Canuto, F. Estrada-Belli, T. G. Garrison, S. D. Houston, M. J. Acuña, et al. Science, 361.6409 (2018): eaau0137.
[9] F. Christnacher, M. Laurenzis, D. Monin, G. Schmitt, N. Metzger, et al., Proc. SPIE 9250, 92500F-1 (2014).
[10] T. Arici, S. Dikbas and Y. Altunbasak, IEEE Trans. Image Process. 18, 1921–1935 (2009).
[11] F. Christnacher, S. Schertzer, N. Metzger, E. Bacher, M. Laurenzis, et al., Opt. Express 23, 32897–32908 (2015).
[12] J. Busck and H. Heiselberg, Appl. Opt. 43, 4705–4710 (2004).
[13] P. Risholm, J. Thorstensen, J. T. Thielemann, K. Kaspersen, J. Tschudi, et al., Appl. Opt. 57, 3927–3937 (2018).
[14] P. Mariani, I. Quincoces, K. Haugholt, Y. Chardard, A. Visser, et al., Sustainability 11, 162 (2019).